Variable stiffness soft pneumatic sensing chambers for tactile sensing and haptic devices

Sensors & Actuators: A. Physical 404 (2026) 117767

Contents lists available at ScienceDirect

Sensors and Actuators: A. Physical

journal homepage: www.journals.elsevier.com/sensors-and-actuators-a-physical

# Variable stiffness soft pneumatic sensing chambers for tactile sensing and haptic devices

Simone Duretto*, Giovanni Colucci, Luigi Tagliavini, Andrea Botta, Giuseppe Quaglia

*Politecnico di Torino, Department of Mechanical and Aerospace Engineering, Corso Duca degli Abruzzi 24, Turin, 10129, Italy*

## HIGHLIGHTS

- Sensing system with variable stiffness using Soft Pneumatic Sensing Chambers (SPSCs).
- Simplified model to correlate the SPSC geometry to the static performance of the system.
- Reliability testing of SPSCs made through Additive Manufacturing and compression molding.
- SPSC as the core element for a tactile system for assistive robotics and a haptic device for human-machine interaction.

## GRAPHICAL ABSTRACT

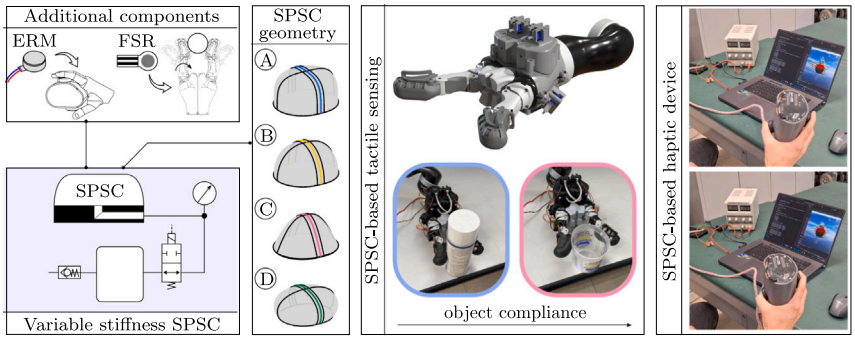


## ARTICLE INFO

*Keywords:*
Soft sensor
Tactile sensing
Human–machine interface
Haptics

## ABSTRACT

This paper discusses the development of a sensing system based on Soft Pneumatic Sensing Chambers (SPSCs) with discretely variable stiffness. The geometric and setup parameters affecting the sensibility and stiffness of the system are first identified through a simplified analytical formulation. Then, a deformation model is implemented to estimate and compare the static performance of four notable SPSC types. Furthermore, SPSCs manufactured through different methods are experimentally characterized in terms of performance and overall reliability. Notably, for SPSC units fabricated from TPU 60A, on average, stiffness increases by 60%, from 5.0 to 8.0 N/mm, when switching between low and high stiffness conditions, while the pressure sensitivity increases more than tenfold, from 0.5 to 6.1 kPa/mm. Furthermore, it is shown that static performance can be accurately predicted across different setup pressures using the geometric data estimated from tests at a single pressure. Finally, two applications are presented, namely, tactile sensing for robotic grasping, and haptic interaction. In these contexts, the advantages of the proposed sensing system over existing solutions are discussed, highlighting the trade-off between functionality and compactness.

## 1. Introduction

Soft Pneumatic Sensing Chambers (SPSCs) are airtight, monolithic, and deformable membranes that function as sensing units in applications requiring a safe and compliant interaction with the environment [33]. They are typically fabricated using easily accessible 3D-printing techniques such as Fused Deposition Modeling (FDM) and Stereolithography (SLA), or by silicone molding. SPSCs are widely appreciated for their inherent compliance, repeatability, and negligible hysteresis. Furthermore, they offer reliability, stability over time, and high durability, while maintaining very low power consumption.

* Corresponding author.
*Email address:* simone.duretto@polito.it (S. Duretto).

https://doi.org/10.1016/j.sna.2026.117767
Received 3 February 2026; Received in revised form 14 March 2026; Accepted 22 March 2026
Available online 23 March 2026

SPSCs are commonly used to measure mechanical inputs such as compression [9,45], rectilinear displacement [38], and bending [34,35,41]. More recently, Ghaffari and Hojjat proposed the use of SPSCs for the measurement of rotational motions [12], and for the simultaneous measurement of linear and rotational displacements [13].

In the fields of robotic manipulation and haptics, SPSCs sensitive to compression are widely adopted as compliant interfaces. For instance, in the case of robotic manipulation it is proven that the interposition of a compliant element between the gripper and the grasped object considerably simplifies the grasping control, which changes from a force control to a position control [44]. Among the most recent examples in this field, Hughes et al. [17] have sensorized a robotic gripper using latex-made SPSCs. Kuppuswamy et al. [23] employed the same material to create soft-bubble fingertips to be mounted on rigid manipulators, whereby the visual monitoring of the internal pattern of the SPSC during gripping is used for in-hand pose estimation and object classification. Another camera-based approach has been proposed by Su et al. [32], who sensorized a silicone-made PneuNet gripper using a soft inflatable palm with internal markers. The DexiTac concept by Lu et al. [24] implements a similar approach for grasping stability assessment. Lastly, Wang et al. [39] developed a rigid-soft gripper where two (or more) soft inflatable bladders are mounted on a rigid cylindrical structure.

On the other hand, in the field of haptic devices, the use of SPSCs enables bi-directional physical interaction with the user. To this aim, Tawk et al. [33] proposed the implementation of different types of SPSCs for rehabilitation, remote control, or generic Virtual Reality (VR) scenarios. More recently, the use of SPSCs has also been proposed for the accurate measurement of forces and torques in applications where a safe and compliant human-machine interaction is required [4,18].

Despite the research efforts in this field, limitations still exist. SPSCs' nominal geometry is limited to spherical caps with limited volumetric deformation when pressurized [33], or flat circular/rectangular membranes that deform upon pressurization [31,37,39]. This results in the absence of a parametric analysis outlining how the SPSC geometry affects the system's static response, here quantified in terms of stiffness and sensitivity. Moreover, the application of variable stiffness SPSCs has been little explored. Indeed, SPSCs are often intended as isolated chambers, where the volume undergoing compression cannot be actively changed. However, such a feature could increase the functionality of SPSC-based systems, allowing for a more rigid or softer interface depending on the needs. Finally, despite recent advancements in the integration of tactile sensing capabilities and haptic feedback in soft robots [28,43], the manufacturing of these integrated sensors often requires specialized processes and equipment, which limits their widespread adoption. Consequently, there is significant value in investigating the integration of off-the-shelf components, which can provide a scalable and accessible pathway to enhanced tactile sensing and haptic feedback.

To partially address these challenges, the authors have previously investigated an SPSC-based system with discretely variable stiffness for robotic tactile sensing and generic Human-Machine Interfaces (HMIs) [5–8], designed to be lightweight, reliable, and low-power.

In this work, we move further by addressing many of the limitations that still affect SPSC-based systems. Specifically, Section 2 resumes the functional design of the variable stiffness SPSC-system and introduces a complete design framework, which includes static performance modeling, a new SPSC geometry definition, and a numerical model to study the SPSC deformation. Section 3 presents the static characterization of different types of SPSC and introduces an experimental identification method to quickly estimate how system performance changes with setup parameters. Notably, on average, a stiffness increase of 60% was recorded, together with a more than tenfold pressure sensitivity increase when switching between low and high stiffness conditions. The reliability of SPSCs fabricated through different manufacturing techniques (FDM, SLA, and compression molding) is also assessed. Finally, Section 4 discusses two applications of variable stiffness SPSCs, i.e., tactile sensing for robotic grasping and haptic interfaces for Human-Machine Interaction.

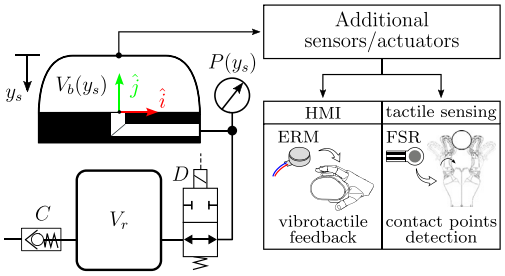


**Fig. 1.** Functional architecture of an SPSC unit with discretely variable stiffness. Advanced functionalities can be achieved by integrating additional sensors and actuators within the SPSC unit.

## 2. Functional design and modeling

The SPSC unit implemented in this work consists of a pressurized deformable bladder that is connected to a pneumatic auxiliary system, as shown in Fig. 1. A directional valve $D$ opens or closes the connection between the bladder volume $V_b$ and a rigid reservoir $V_r$. Practically, the system behaves as a pneumatic spring with discretely tunable stiffness, in which the air volume that undergoes deformation is controlled through a directional valve.

The check valve $C$ allows pressure to be retained in the system, effectively making it a closed system. While the system is inherently designed to function without initial pressurization, an optional configuration phase can be implemented. During this phase, the system is pressurized using an external compressor, which is subsequently disconnected before operation commences. This design choice results in a lighter system by eliminating the need for an onboard compressor while still enabling the pre-adjustment of the interaction force prior to putting the system into operation.

Finally, a pressure sensor allows for indirect measurement of the interaction force between the environment and the SPSC, and the amount of squeezing undergone by the SPSC is described by the contact depth $y_s$.

As will be illustrated in Section 4, depending on the application, the SPSC functionality can be further extended by integrating additional sensors and/or actuators within the bladder. For instance, in robotic tactile sensing, capacitive, resistive, or vision-based sensors can be used to recognize contact points, while in HMIs, vibrating actuators (e.g., ERMs, LRAs, piezoelectric benders) provide localized vibrotactile feedback.

### 2.1. SPSC sensibility and stiffness

The contact force generated on the object interacting with the SPSC depends on the structural stiffness of the bladder, as well as on the air spring and object stiffnesses. For modeling purposes, the following simplifying assumptions are made:

- the SPSC and the air spring are modeled as two springs acting in parallel;
- the contact object is an infinitely rigid plate uniformly squeezing the SPSC along axis $\hat{j}$ (see Fig. 1).

It is worth noting that the term *mechanical compliance* traditionally describes a spring-damper system [16], with the damping component being critical for high-speed dynamics and impact mitigation [1,3]. However, in the field of Service Robotics, compliance is often reduced to describing only the static stiffness due to the relatively slow dynamics [9,23,37]. Therefore, in the following, slow dynamics will be assumed and only the static performance of the system will be considered.

Under these assumptions, let $F(y_s)$ be the interaction force between the bladder and the rigid plate:

$$F(y_s) = F_{el}(y_s) + \left(P(y_s) - P_{amb}\right)\, A(y_s) \tag{1}$$

where $F_{el}(y_s)$ is the elastic reaction force of the SPSC coming from its structural stiffness, $A(y_s)$ is the contact area, $P_{amb}$ is the ambient pressure, and $P(y_s)$ is the absolute pressure in the bladder. The latter can be described by the polytropic law:

$$P(y_s) = P_i \left(\frac{V_i}{V(y_s)}\right)^n \tag{2}$$

where $n$ is the polytropic index. $V_i$ is the volume of air in the rest state, which depends on the switching state of the directional valve:

$$V_i = \begin{cases} V_{b,i}, & \text{closed valve} \\ V_{b,i} + V_r, & \text{open valve} \end{cases} \tag{3}$$

with $V_{b,i}$ defined as the internal volume of the bladder in the undeformed configuration. The volume in the rest state can also be expressed in terms of a dimensionless parameter $\xi$, defined as follows:

$$\xi = \frac{V_i}{V_{b,i}} \geq 1 \tag{4}$$

The volume $V(y_s)$ will instead be equal to:

$$V(y_s) = V_i - \Delta V(y_s) \tag{5}$$

where $\Delta V(y_s)$ is the air volume change during contact.

In general, $\Delta V(y_s)$ and $A(y_s)$ also depend on the geometry and stiffness of the object that interacts with the SPSC. However, under the simplifying assumption introduced above, these quantities depend only on the geometry of the SPSC and can therefore be regarded as geometric parameters.

Finally, $P_i$ is the pressure of the system at rest, set by the pressure source during the initial setup.

Thus, it is possible to rewrite (1) and (2) as follows:

$$P(y_s) = P_i \left(\frac{\xi\, V_{b,i}}{\xi\, V_{b,i} - \Delta V(y_s)}\right)^n \tag{6}$$

$$F(y_s) = F_{el}(y_s) + \left(P(y_s) - P_{amb}\right)\, A(y_s) \tag{7}$$

The first-order derivatives of $P(y_s)$ and $F(y_s)$ with respect to the contact depth $y_s$ are of particular interest. The former represents the sensitivity of the sensing unit, while the latter represents the stiffness of the sensing system:

$$\frac{dP}{dy_s} = \frac{dP}{d\Delta V}\,\frac{d\Delta V}{dy_s} = \frac{n\, P(y_s)\, A(y_s)}{\xi V_{b,i} - \Delta V}\,\frac{d\Delta V}{dy_s} \tag{8}$$

$$\frac{dF}{dy_s} = k_{el}(y_s) + \left(P(y_s) - P_{amb}\right)\,\frac{dA}{dy_s} + \frac{dP}{dy_s}\,A(y_s) \tag{9}$$

With respect to (9), the first term represents the structural stiffness of the membrane, the second term is related to the variation of the contact area, while the latter term is related to the variation of the volume, which is linked to the sensitivity. Eqs. (6–9) show that both the geometric parameters $\{V_{b,i},\, \Delta V(y_s),\, A(y_s),\, d\Delta V/dy_s,\, dA/dy_s\}$ and the setup parameters $\{P_i,\, \xi\}$ influence the static performance of the sensing system.

### 2.2. SPSC geometry definition

While the effect of $P_i$ and $\xi$ on the static performance is easily understood, i.e., by increasing the pressure or reducing the value of $\xi$ it is possible to increase stiffness and sensitivity, it is also of interest to analyze the effect of the SPSC geometry. In fact, there are no studies in the literature that analyze the influence of the nominal geometry of the SPSC on its behavior, which is generally assumed to have a spherical cap shape [32,33,37]. Moreover, the analysis of alternative geometries is intriguing in order to easily accommodate additional sensors/actuators within the SPSC unit.

The geometry of a generic SPSC can be schematized as shown in Fig. 2(a). In the mid-plane $\hat{\imath} - \hat{\jmath}$ the cross section is described by a *generalized super-ellipse* curve [26] with parametric equations:

$$X(u) = \bar{w}\,[\sin(u)]^{\,2/n_1}\,\mathrm{sgn}(\sin(u)) \tag{10}$$

$$Y(u) = \bar{h}\left([\cos(u)]^{\,2/n_2}\,\mathrm{sgn}(\cos(u)) + c_y\right) \tag{11}$$

where $u \in [-\pi + \Delta u, \pi - \Delta u]$ is the angle measured from positive $\hat{\jmath}$ direction, increasing clockwise. The quantities $\Delta u$, $\bar{w}$ and $\bar{h}$ are defined as follows:

$$\Delta u = \mathrm{acos}\left(\left|-c_y\right|^{n_2/2}\right) \tag{12}$$

$$\bar{h} = \frac{h}{1 + c_y} \tag{13}$$

$$\bar{w} = \frac{w}{[\sin(\Delta u)]^{2/n_1}} \tag{14}$$

with $w$ and $h$ representing, respectively, the encumbrance at the fixed edge and the height of the cross section, while $\{n_1,\, n_2,\, c_y\}$ are

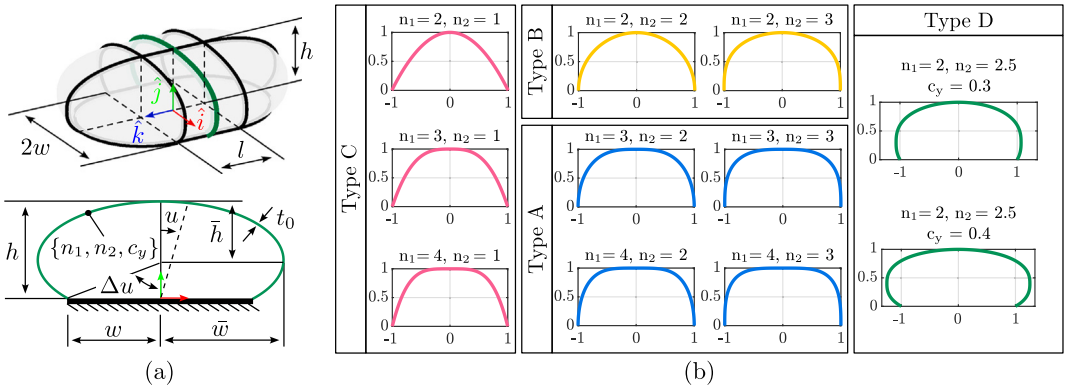


**Fig. 2.** (a) Geometry of a generic SPSC and identification of its parameters. The cross section in the mid-plane $\hat{\imath} - \hat{\jmath}$ is represented as a generalized super-ellipse curve. (b) SPSC cross sections for different combinations of $\{n_1,\, n_2,\, c_y\}$, with unitary semi-axes $w$ and $h$. Four notable SPSC families (namely A, B, C, D) are identified.

used as control parameters to change the shape of the cross section. Specifically:

1. $\{n_1, n_2\} \geq 1$: these parameters control the roundness of the cross section. Specifically, increasing $n_1$ makes the top surface flatter, while increasing $n_2$ makes the lateral surface more vertical;
2. $c_y \geq 0$: this parameter translates the super-ellipse along $\hat{j}$, and ultimately controls the SPSC bulging.

According to the combination of the parameters $\{n_1, n_2, c_y\}$ four notable SPSC types can be identified (Fig. 2(b)):

1. Type A: $n_1 \geq 3$, $n_2 \geq 2$, $c_y = 0$
2. Type B: $n_1 = 2$, $n_2 \geq 2$, $c_y = 0$
3. Type C: $n_1 \geq 2$, $n_2 = 1$, $c_y = 0$
4. Type D: $n_1 = 2$, $n_2 \geq 2$, $c_y > 0$

Regarding the reasons behind this classification, note that Type A has sidewalls that tend to be vertical and the top wall that tends to be flat, Type B is the one that resembles a spherical cap, Type C has sloped sidewalls, while Type D has bulging sidewalls.

Thus, the SPSC is obtained by first thickening the cross section defined above by a quantity $t_0$, then extruding the profile along $\hat{k}$ for a length $l$, with $\hat{i} - \hat{j}$ as the mid-plane. To complete the geometry, revolute extrusions are performed on both sides of the SPSC.

In the end, the SPSC geometry is completely described by a set of seven parameters, namely:

- $w$, $h$, $l$: these parameters define the encumbrance of the SPSC, as shown in Fig. 2;
- $t_0$: thickness of the SPSC membrane. The minimum thickness is mainly influenced by manufacturing technology (e.g., in Additive Manufacturing, it is impractical to produce bladders with a thickness less than 0.8 mm) and by ensuring the air-tightness of the SPSC unit. At the same time, the thickness cannot be too large, to limit the structural stiffness of the bladder;
- $n_1$, $n_2$, $c_y$: form factors defining the shape of the SPSC, as shown above.

This description of the geometry is particularly convenient: indeed, it can be used to implement a structural model of the SPSC to predict its deformation both during inflation and under contact with an object, as will be illustrated in the next Subsection.

### 2.3. SPSC deformation model

The general method for modeling the deformation of non-linear axisymmetric membranes was first presented by Yang and Feng [42]. This approach transforms a boundary-value problem into an initial value problem, allowing to obtain the solution using standard numerical methods for the integration of ODEs. The same authors utilized this technique to study the contact problem of inflated spherical non-linear membranes [10]. More recently, other authors have used the same method to study the forced compression of inflated ellipsoidal membranes [29,30].

In the following, the method presented in [42] will be applied to model the deformation of a generic SPSC, both during the inflation process and when compressed by an infinitely rigid plate. Specifically, the deformed cross section in the revolute portion of the SPSC will be analyzed using this approach. Subsequently, it will be assumed that the SPSC has the same deformed cross section in the extruded part. In previous works, the authors simplified the SPSC deformed configuration by considering the intersection between the nominal SPSC and a contact plate [6]. That approach neglected the bulging of the lateral surface during contact and did not accurately capture the behavior of the contact force. On the contrary, the approach herein adopted enables a more precise evaluation of the SPSC static performance, avoiding the complexity of full multiphysics FEM analyses.

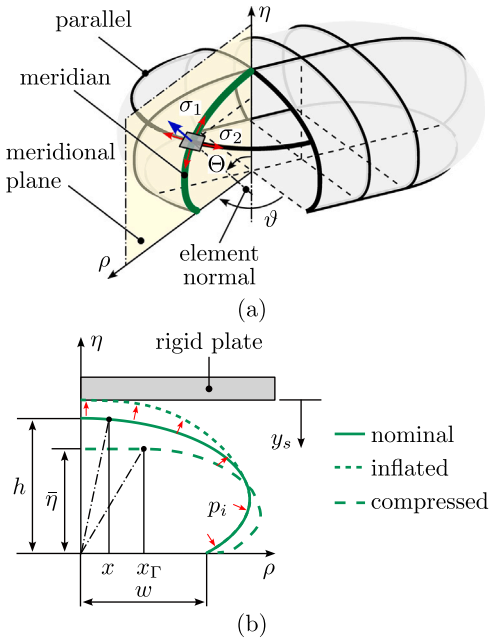


**Fig. 3.** Structural analysis of the revolute part of the SPSC. (a) Identification of the generic section on a meridional plane. (b) SPSC half-section on the meridional plane. The SPSC is first inflated at gauge pressure $p_i$, then it is compressed by an infinitely rigid plate.

#### 2.3.1. Preliminary definitions

As shown in Fig. 3, in the nominal configuration the revolute part of the SPSC is described by the set of cylindrical coordinates $(x, y, \vartheta)$, while in the deformed configuration the set of coordinates becomes $(\rho(x), \eta(x), \vartheta)$. $x$ is taken as the independent variable, with all derivatives evaluated with respect to it. Moreover, subscripts $[\cdot]_1$ and $[\cdot]_2$ will be used to denote the meridional and the circumferential directions of the deformed membrane, respectively.

The explicit equation of the super-ellipse for $x > 0$ is as follows:

$$y = \pm \bar{h} \left[ \left( 1 - \left( \frac{x}{\bar{w}} \right)^{n_1} \right)^{1/n_2} + c_y \right] \tag{15}$$

Eq. (15) can be derived with respect to $x$ to get:

$$g(x) = y' = \mp \frac{\bar{h}}{\bar{w}} \frac{n_1}{n_2} \left( \frac{x}{\bar{w}} \right)^{n_1 - 1} \left( 1 - \left( \frac{x}{\bar{w}} \right)^{n_1} \right)^{1/n_2 - 1} \tag{16}$$

In (16) the minus sign refers to the super-ellipse portion corresponding to $y \geq c_y \bar{h}$, while the plus sign refers to the part with $y < c_y \bar{h}$.

In the meridional plane, the infinitesimal arc lengths in the undeformed and deformed configurations are respectively:

$$ds = \left( dx^2 + dy^2 \right)^{1/2} = \left( 1 + g^2 \right)^{1/2} dx \tag{17}$$

$$dS = \left( d\rho^2 + d\eta^2 \right)^{1/2} = \left( \rho'^2 + \eta'^2 \right)^{1/2} dx \tag{18}$$

Thus, the principal stretch ratios are:

$$\lambda_1 = \frac{dS}{ds} = \left( \frac{\rho'^2 + \eta'^2}{1 + g^2} \right)^{1/2} \tag{19}$$

$$\lambda_2 = \frac{\rho}{x} \tag{20}$$

$$\lambda_3 = \frac{t}{t_0} = \frac{1}{\lambda_1 \lambda_2} \tag{21}$$

Eq. (21) arises from the hypothesis of material incompressibility. $t_0$ and $t$ are, respectively, the thicknesses of the undeformed and deformed membrane.

The forces per unit length are obtained from the true stresses in the membrane, under the hypothesis of biaxial loading:

$$T_1 = t\sigma_1 = 2t_0\left(\frac{\lambda_1}{\lambda_2} - \frac{1}{\lambda_1^3\lambda_2^3}\right)\left(\frac{\partial W}{\partial I_1} + \lambda_2^2\frac{\partial W}{\partial I_2}\right) \tag{22}$$

$$T_2 = t\sigma_2 = 2t_0\left(\frac{\lambda_2}{\lambda_1} - \frac{1}{\lambda_1^3\lambda_2^3}\right)\left(\frac{\partial W}{\partial I_1} + \lambda_1^2\frac{\partial W}{\partial I_2}\right) \tag{23}$$

where $W$ is the strain energy density function, which depends on the hyperelastic model adopted, while $I_1$ and $I_2$ are, respectively, the first and second strain invariants:

$$I_1 = \lambda_1^2 + \lambda_2^2 + \frac{1}{\lambda_1^2\lambda_2^2}, \quad I_2 = \frac{1}{\lambda_1^2} + \frac{1}{\lambda_2^2} + \lambda_1^2\lambda_2^2 \tag{24}$$

For convenience, the following auxiliary variable is defined:

$$\delta = \rho' = \frac{d}{dx}\left(\lambda_2 x\right) \tag{25}$$

Lastly, the derivative of the deformed membrane height, obtained by reworking (19), is:

$$\eta' = -\left[\lambda_1^2\left(1+g^2\right) - \delta^2\right]^{1/2} \tag{26}$$

It should be noted that the minus sign is necessary as $\eta(x)$ decreases when $x$ increases.

### 2.3.2. Problem formulation

The equilibrium equations for membranes of revolution in the meridional section, along tangential and normal directions, are:

$$\frac{dT_1}{d\rho} + \frac{1}{\rho}\left(T_1 - T_2\right) = \frac{p_t}{\cos\Theta} = 0 \tag{27}$$

$$k_1T_1 + k_2T_2 = p_n \tag{28}$$

where $p_t$ and $p_n$ are the loads acting on the deformed surface in the meridional normal and tangential directions. Specifically, in (27) $p_t$ is set to zero, i.e., it is assumed there is no friction between the membrane and the contact object (if present), while in (28) $p_n = p = P - P_{amb}$ is the gauge pressure inside the bladder. $k_1$ and $k_2$ are the principal curvatures, defined as follows:

$$k_1 = \frac{d\Theta}{dS} = \frac{-\left(\rho'\eta'' - \rho''\eta'\right)}{\left(\rho'^2 + \eta'^2\right)^{3/2}} \tag{29}$$

$$k_2 = \frac{\sin\Theta}{\rho} = \frac{\eta'}{\rho\left(\rho'^2 + \eta'^2\right)^{1/2}} \tag{30}$$

with $\cos\Theta = d\rho/dS$ and $\sin\Theta = d\eta/dS$.

By reworking (25), (27) and (28) a system of three ODEs is obtained, which can be used to study the membrane deformation in the free and contact regions.

In the free surface, the system of ODEs is defined as follows:

$$\begin{cases} \lambda_1' = \dfrac{\lambda_2 - \delta}{x}\dfrac{f_2}{f_1} - \dfrac{\delta}{\lambda_2 x}\dfrac{f_3}{f_1} \\ \lambda_2' = \dfrac{\delta - \lambda_2}{x} \\ \delta' = \dfrac{-p\,\lambda_1\left(1+g^2\right)^{1/2}\left[\lambda_1^2\left(1+g^2\right) - \delta^2\right]^{1/2}}{T_1} \\ \qquad - \dfrac{\lambda_1^2\left(1+g^2\right) - \delta^2}{\lambda_2\,x}\dfrac{T_2}{T_1} + \dfrac{\delta\lambda_1'}{\lambda_1} + \dfrac{\delta g g'}{1+g^2} \end{cases} \tag{31}$$

where $f_1 = \partial T_1/\partial\lambda_1$, $f_2 = \partial T_1/\partial\lambda_2$, and $f_3 = T_1 - T_2$. The above system of ODEs is defined in the interval $0 \le x \le w$ for the inflation problem, and $x_\Gamma \le x \le w$ for the contact problem, with $x_\Gamma$ representing the boundary of the contact region.

In the contact region the surface is flattened, i.e., $\eta' = 0$. Hence:

$$\delta = \lambda_1\left(1+g^2\right)^{1/2} \tag{32}$$

Thus, the set of ODEs reduces to the following:

$$\begin{cases} \lambda_1' = \dfrac{\lambda_2 - \lambda_1\left(1+g^2\right)^{1/2}}{x}\dfrac{f_2}{f_1} - \dfrac{\lambda_1\left(1+g^2\right)^{1/2}}{\lambda_2 x}\dfrac{f_3}{f_1} \\ \lambda_2' = \dfrac{\lambda_1\left(1+g^2\right)^{1/2} - \lambda_2}{x} \end{cases} \tag{33}$$

The last system of ODEs is defined in the interval $0 \le x \le x_\Gamma$.

The boundary conditions for (31) and (33) are defined to:

1. ensure the continuity of the solution between the contact and free surfaces at $x = x_\Gamma$;
2. impose that no deformation along $x$ occurs at the bottom fixed edge $x = w$.

Moreover, from (19), (20), (25), it can be easily demonstrated that the solution at $x = 0$ is $\lambda_1 = \lambda_2 = \delta = \lambda_0$, where $\lambda_0$ is a parameter that needs to be guessed, as will be discussed below. Thus, the boundary conditions for the inflation and contact problem are:

*Inflation Problem*

$$\begin{aligned} &x = 0 \quad && \lambda_1 = \lambda_2 = \delta = \lambda_0 \\ &x = w \quad && \lambda_2 = 1 \end{aligned}$$

*Contact Problem*

$$\begin{aligned} &x = 0 \quad && \lambda_1 = \lambda_2 = \delta = \lambda_0 \\ &x = x_\Gamma \quad && \lambda_{1,\text{contact}} = \lambda_{1,\text{free}},\ \lambda_{2,\text{contact}} = \lambda_{2,\text{free}}, \\ & && \delta_{\text{contact}} = \delta_{\text{free}} \\ &x = w \quad && \lambda_2 = 1 \end{aligned}$$

The analysis of Type D geometry requires particular attention. As a matter of fact, the system of ODEs for the free surface must be split into two intervals, i.e., $0 \le x \le \bar{w}$ and $\bar{w} > x \ge w$. The first one covers the range $\eta(x_\Gamma) \ge y > c_y\bar{h}$, with $g(x)$ inserted in (31) with negative sign. The second part addresses $c_y\bar{h} > y \ge 0$, using the positive sign for $g(x)$. To maintain the continuity of the solution, the final values $\{\lambda_1(x=\bar{w}), \lambda_2(x=\bar{w}), \delta(x=\bar{w})\}$ from the first part serve as the initial values for the second part. Also, notice that the second part is solved in reverse order, that is, for decreasing values of $x$.

For the contact problem, a constraint on the volume of the deformed SPSC is required [10,29,30]. In this case, the constraint is derived from the polytropic law:

$$V = V_i\left(\frac{P_i}{P}\right)^{1/n} \tag{34}$$

where $V_i$ and $V$ are respectively the volumes of the SPSC after inflation and during compression, $P_i$ is the absolute inflation pressure, $P$ is the absolute pressure during compression, and $n$ is the polytropic index ($n = 1$ for an isothermal process).

Once the solution $\{\lambda_1(x), \lambda_2(x), \delta(x)\}$ is obtained, the deformed configuration $(\rho(x), \eta(x))$ can be easily derived:

$$\rho(x) = \lambda_2 x \tag{35}$$

$$\eta(x) = \int -\left[\lambda_1^2\left(1+g^2\right) - \delta^2\right]^{1/2} dx \tag{36}$$

**Algorithm 1** Numerical procedure for the solution of the Inflation and Contact problems.

**Input:** Gauge pressure $p$
**Result:** Principal stretches $\lambda_{1,2}$ at equilibrium
**if** *Contact Problem* **then**
  Initial guess for contact boundary $x_\Gamma$
**end**
**while** *Constraints not satisfied* **do**
  Initial guess for $\lambda_0$
  **while** $\lambda_2(w) \neq 1$ **do**
    Solve ODEs (31) and (33)
    **if** $\lambda_2(w) \approx 1$ **then**
      **break** (solution found for current $x_\Gamma$)
    **else**
      Increase $\lambda_0$
      **if** $\lambda_0 > \lambda_{0,thr}$ **then**
        **break** (threshold exceeded)
      **end**
    **end**
  **end**
  **if** *Contact Problem* ***and*** *(Volume Constraint not satisfied* ***or*** $\lambda_0 > \lambda_{0,thr}$*)* **then**
    Increase guess for $x_\Gamma$
  **else**
    **Terminate** (Solution converged)
  **end**
**end**

for $0 \leq x \leq w$. The height of the deformed SPSC, i.e., $\eta(0)$, is denoted as $\bar{\eta}$. Then, the volume of the deformed SPSC can be computed as:

$$V = \pi \int_0^{\bar{\eta}} \rho^2 d\eta + 2l \int_0^{\bar{\eta}} \rho d\eta \tag{37}$$

On the other hand, the contact area $A$ is simply given by:

$$A = \pi x_\Gamma^2 + 2x_\Gamma l \tag{38}$$

The numerical procedure to solve (31) and (33) is summarized in Algorithm 1, and it is implemented by the authors in a Matlab code, which is distributed as open-source.[1]

#### 2.3.3. Discussion

Fig. 4 shows the results obtained from the deformation model illustrated above for SPSCs with $h = w = l = 10$ mm and $t_0 = 1$ mm. The super-ellipse coefficients for the different types are given in Fig. 4. The selected material is cured Formlabs Elastic 50A, for which a hyperelastic Yeoh 3rd order model is found in the literature [40]. In this analysis, the SPSCs have been first inflated ($p_i = 10$ kPa), then compressed by a rigid plate. For the low stiffness condition, the dimensionless parameter $\xi$ has been set to 6 for all SPSCs.

Fig. 4(a) depicts the deformed configurations, i.e., the inflated and the compressed ones, in the high stiffness configuration. It must be noted that a small tolerance on the boundary condition $\lambda_2(x = w) = 1$ has been set to enforce convergence of the results. The inflation process deforms the nominal geometry, thus increasing the volume of the SPSC.

As expected, SPSCs with flatter top surfaces (Types A and D) or semicircular profiles (Type B) exhibited significant deformation during inflation. For these Types, the volume increase ranged from 5% to 14% across two different geometry sets: the first one, denoted as GS1, was introduced in this Section, while the other one, denoted as GS2, will be introduced in Section 3. Specifically, Type A showed an expansion between 5.2% (GS1) and 13.9% (GS2), Type B varied between 5.6% (GS2) and 10.5% (GS1), while Type D spanned between 7.5% (GS2) and 12.6% (GS1). In contrast, Type C showed negligible deformation (0.1%, data available only for GS1). From the results obtained for GS1 and GS2, an average increase in bladder volume between nearly 0% and 10% can generally be expected.

A comparison between the implemented deformation model and the simplified one (i.e., the volume intersection of the nominal SPSC and the contact plate) is given in Figs. 4(b) and (c) for the two working modes. As can be seen, the bulging of the lateral walls radically changes the expected static performance of the SPSC unit, and this is particularly critical in the high stiffness condition, where the involved volumes are smaller.

## 3. Experimental testing

In this Section, the results of the static characterization of the four SPSC types will be illustrated. The reliability of SPSCs fabricated through different manufacturing processes will also be assessed.

### 3.1. Static characterization

Fig. 5(a) shows the experimental setup used for the static characterization of the SPSCs. Specifically, the SPSC is connected to a rigid reservoir, and a pressure transducer (Honeywell ABPDANN030PGAA5, F.S. 207 kPa gauge, accuracy ±0.25%) reads the pressure inside the chamber. A rigid plate, constrained by a linear guide to translate along $\hat{j}$ only, uniformly squeezes the membrane. A load cell (LCM Systems DCE-500 N, F.S. 500 N, non-linearity ±0.25%) reads the value of the pressing force $F(y_s)$. The results presented herein have been obtained for SPSCs made of TPU 60A (by Recreus), with $h = 13$ mm, $w = 11$ mm, $l = 3$ mm, and $t_0 = 1$ mm. The remaining geometric parameters are summarized in Table 1, while the details about the fabrication of the SPSCs are given in Appendix D of supplementary material S1.

The elastic force $F_{el}(y_s)$ of each SPSC type has been characterized by performing a squeeze-release cycle starting from the rest configuration $y_s = 0$, with the SPSC open to atmosphere. A hysteretic behavior was observed, with a maximum hysteresis of 8.1 N for Type A, 3.8 N for Type B, 4 N for Type C, and 4.5 N for Type D. Hysteresis curves are provided in Appendix A of supplementary material S1, while in Fig. 5(b) the average value of $F_{el}(y_s)$ over the cycle is reported. As can be seen, Types B and C exhibit an initial interval with moderate slope, a central phase with nearly zero slope, and a final interval with high slope. On the other hand, Type A presents a similar behavior, but without the nearly zero slope central phase. For these three types, the final stiffening phase is due to the activation of edge stiffness, which is caused by the bulging of the lateral walls. Conversely, Type D shows a significantly less pronounced stiffening behavior due to its already bulged lateral walls.

The static characterization has been repeated for setup pressures in the range $p_i \in [10, 40]$ kPa (gauge), and by considering both low and high stiffness SPSC configurations. For the low stiffness condition, the SPSCs were connected to a rigid reservoir with volume $V_r = 40$ cm$^3$. As an example, Fig. 5(c) and (d) report the results for the tests at $p_i = 40$ kPa in the high stiffness condition. Results for different setup pressures are given in Appendix B of supplementary material S1. Starting from these tests, by reworking Eqs. (6–7) one can estimate the contact area $A(y_s)$ and the volume change $\Delta V(y_s)$:

$$A(y_s) = \frac{F(y_s) - F_{el}(y_s)}{P(y_s) - P_{amb}} \tag{39}$$

$$\Delta V(y_s) = \xi V_{b,i} \left[ 1 - \left( \frac{P_i}{P(y_s)} \right)^{1/n} \right] \tag{40}$$

where $P(y_s)$ and $F(y_s)$ are the quantities measured during the static tests, while $F_{el}(y_s)$ is previously determined as illustrated above and it is assumed to be independent of pressure in the bladder. Due to the static testing condition, an isothermal process is assumed ($n = 1$).

[1] https://github.com/seromedises-PoliTo/VSSPSC.git

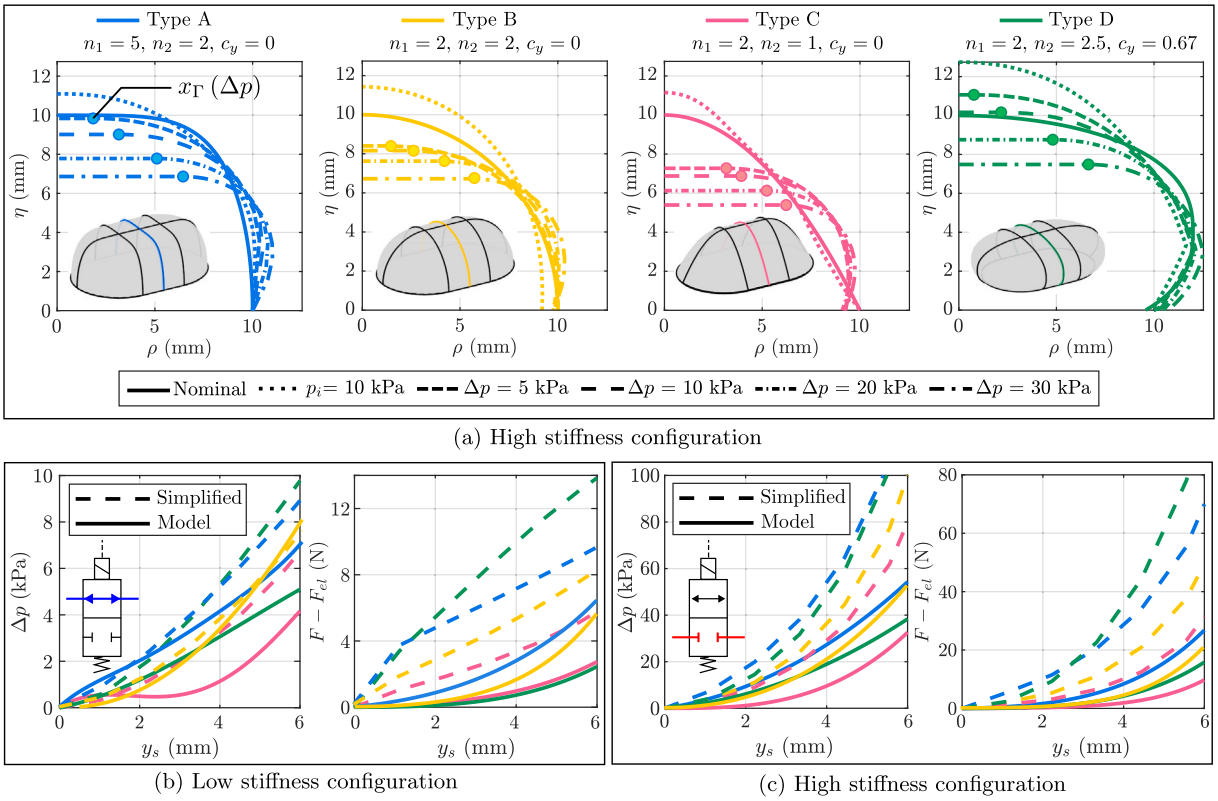


**Fig. 4.** (a) Deformed configurations of SPSCs in the high stiffness configuration. The SPSC is initially inflated, then uniformly compressed by a rigid plate. (b–c) Comparison between simplified model and deformation model, in the (b) low stiffness and (c) high stiffness configurations. SPSCs made of Formlabs Elastic 50A, with $h = w = l = 10$ mm, $t_0 = 1$ mm, and setup pressure $p_i = 10$ kPa.

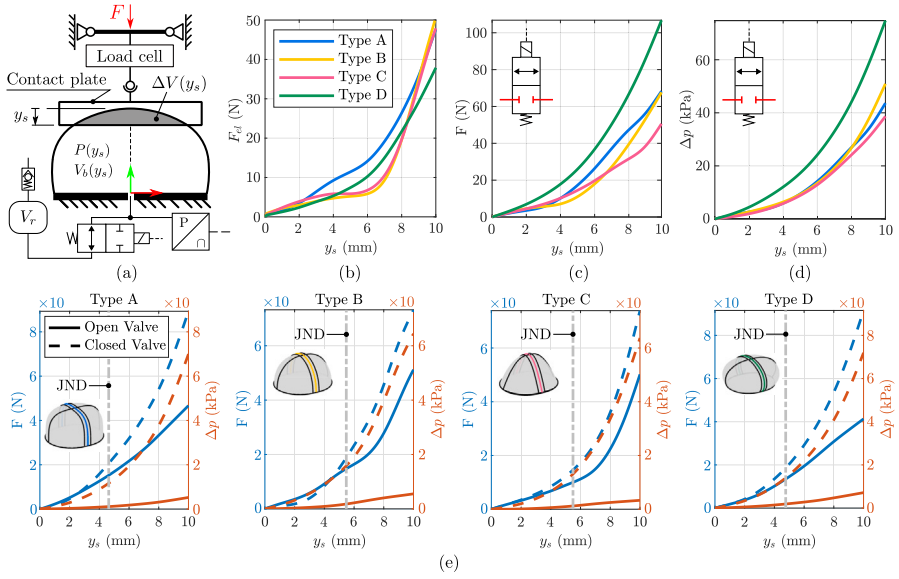


**Fig. 5.** Static characterization of the four notable SPSC types identified, with specimens made of TPU 60A material and manufactured through FDM. (a) Experimental setup. (b) SPSC average elastic force over a squeezing cycle, measured with the chamber open to the atmosphere. (c) Contact force, and (d) pressure change in the SPSC, measured with the SPSC chamber isolated ($p_i = 40$ kPa gauge). (e) Comparison of contact forces and pressure changes in the low and high stiffness configurations ($p_i = 10$ kPa gauge, $V_r = 40$ cm$^3$). Highlighted is the contact depth $y_s$ at which a *just noticeable difference* (JND) in force can be detected between the two conditions.

Notably, the variation span for the experimental values of $A(y_s)$ and $\Delta V(y_s)$ is relatively small. As an example, Fig. 6(a), (b) shows the estimated $A(y_s)$ and $\Delta V(y_s)$ for the Type D SPSC in the low stiffness condition. As a consequence, it is possible to estimate $A(y_s)$ and $\Delta V(y_s)$ by performing a test at a given setup pressure, then use these quantities to estimate $P(y_s)$ and $F(y_s)$ at different setup pressures using Eqs. (6–7). The result of this procedure for the Type D SPSC is shown in Fig. 6(c) and (d). In this case, the data from the test at $p_i = 40$ kPa are used to estimate $A(y_s)$ and $\Delta V(y_s)$. The complete results for Types A, B,

**Table 1**
Parameters of the SPSCs considered in the static characterization. The four types have the same footprint ($w$ = 11 mm, $h$ = 13 mm, $l$ = 3 mm) and wall thickness ($t_0$ = 1 mm).

| Type | $n_1$ | $n_2$ | $c_y$ | $V_{b,i}$ (cm$^3$) |
|---|---|---|---|---|
| A | 3 | 4 | 0 | 4.96 |
| B | 2 | 2.2 | 0 | 4.09 |
| C | 2 | 1 | 0 | 3.04 |
| D | 2 | 2.2 | 0.6 | 6.50 |

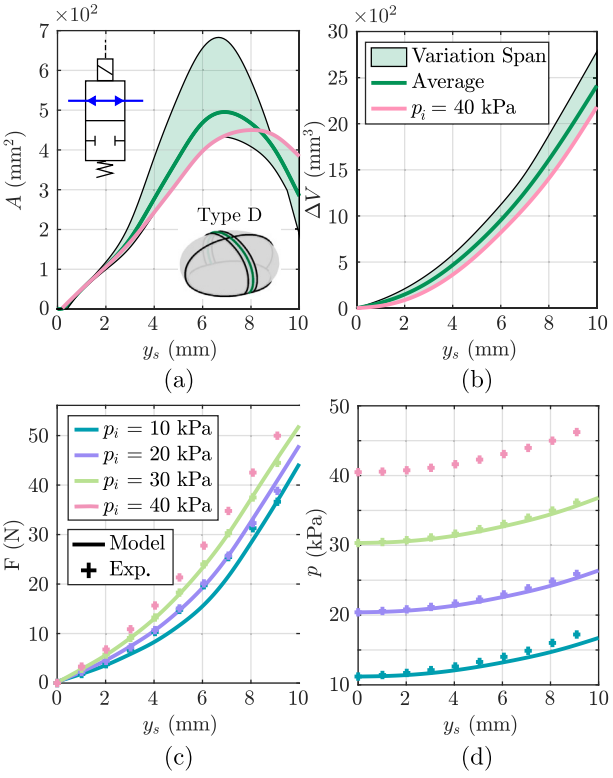


**Fig. 6.** (a) Contact area and (b) volume change of a Type D SPSC estimated from the static test data, with $p_i \in [10, 40]$ kPa and low stiffness configuration. (c) Contact force and gauge pressure estimated starting from the static test at $p_i$ = 40 kPa in the low stiffness configuration.

C, D in the low and high stiffness configurations are given in Appendix C of supplementary material S1.

As shown in Fig. 5(c) and (d), in terms of overall contact force $F(y_s)$ Type C shows the lowest values among all SPSCs. Indeed, despite a higher structural stiffness, Type C shows a smaller contact area (see Fig. 7(a)). On the other hand, Type D exhibits a higher contact force due to its larger contact area. Finally, Types A and B present similar contact forces, with Type A showing slightly higher values due to its higher structural component. In terms of pressure sensitivity, Types A, B and C are substantially similar in the high stiffness configuration. At last, Type D shows the highest pressure sensitivity, which is motivated by a higher volume change with respect to the other types (see Fig. 7(b)).

In the end, Type D is preferable when high sensitivity and high contact forces are required, while Type C is preferable when low contact forces are needed. Type B is suitable when a sudden change in stiffness is required around half of the contact stroke. Instead, the behavior of the contact force for Type A is a compromise between Types B and D. The features of Types A, B, and C come at the cost of a lower sensitivity compared to Type D.

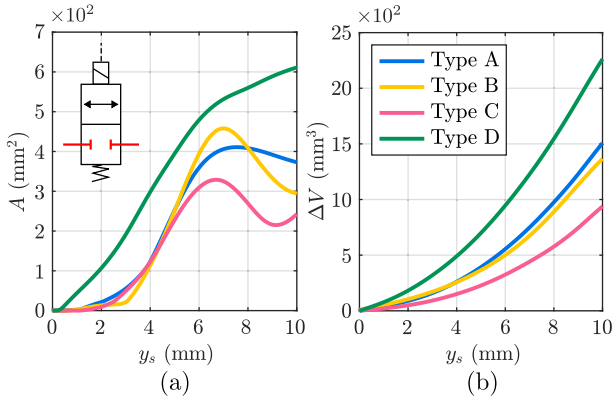


**Fig. 7.** Comparison of estimated (a) contact area and (b) volume change for the four SPSC types. The values are averaged from static tests performed in the high stiffness configuration, with $p_i \in [10, 40]$ kPa.

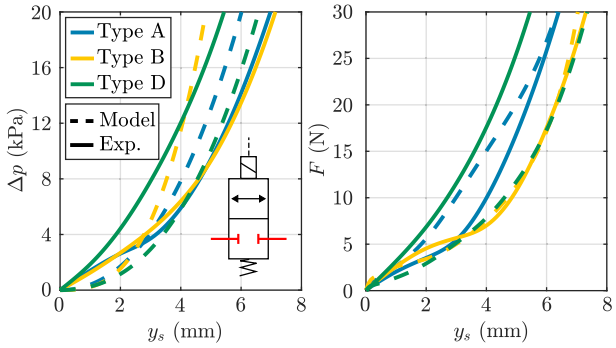


**Fig. 8.** Comparison between estimated and measured static performance for three SPSC types, in the high stiffness configuration. Geometric parameters are given in Table 1. $p_i$ = 40 kPa.

The effectiveness of the stiffness variation between the two working conditions was evaluated using the *just noticeable difference* (JND) metric [20], which represents the minimum difference in force stimulus that a human can reliably perceive. Specifically, for contact forces, a relative discrimination threshold of 10% was set, combined with an absolute discrimination threshold of 5 N. As shown in Fig. 5(e), for all SPSC Types the JND is around 5 mm, with Types A and D performing slightly better than Types B and C. It was observed that, on average, the stiffness increased by 60%, from 5.0 N/mm to 8.0 N/mm when switching from low to high stiffness condition. Simultaneously, pressure sensitivity increased more than tenfold, from 0.5 kPa/mm to 6.1 kPa/mm. These results represent global mean values across all four Types; they were calculated by first averaging the performance of each SPSC Type across its $y_s$ range and for internal pressures $p_i \in [10, 40]$ kPa (gauge).

Fig. 8 shows a comparison between the experimental static performance and the one estimated through the numerical model presented in Section 2.3, for Types A, B and D SPSCs in the high stiffness configuration. SPSCs properties are the same as those characterized above, and the inflation pressure is set to $p_i$ = 40 kPa. In this instance, the material model has been linearized (i.e, Hooke's law is used), with Young modulus estimated from the material manufacturer's datasheet ($E$ = 5 MPa, considering the stress at 20% elongation) and Poisson ratio chosen close to the incompressibility condition ($\nu$ = 0.49). Moreover, the contact force from the numerical model has been summed with the experimental elastic reaction force before comparing it to the experimental contact force, to provide a more direct comparison. Overall, for Types A and B the contact forces present a good match, while the estimated pressure change shows a higher deviation, with the estimates lower than the

measured values at low strokes, while the opposite behavior is observed at higher strokes. This is likely due to the overestimate of the inflated volume at low strokes and the neglect of border effects at higher strokes. Conversely, for Type D both estimated quantities are lower than the measured ones, which is likely motivated by an overestimate of the inflated volume. Finally, it was observed that for this particular combination of SPSC geometry and material, convergence of the numerical model cannot be guaranteed for Type C geometry.

### 3.2. Reliability testing

The sensing unit presented here is based on a closed, pressurized pneumatic system, and any damage to the SPSC would significantly damage its operation. Therefore, the assessment of SPSC reliability is of particular interest, and it was tested here through a leakage test, a fatigue test, and a puncture test.

As regards the leakage test, the SPSCs were first inflated to a pressure of $p_i = 40$ kPa (gauge) and then isolated from the supply source. The test is passed if the SPSC is leak-free for at least 30 minutes, according to [33]. No significant leakages were detected for SLA-printed bladders, while FDM-printed bladders showed minor leakages (<1 kPa) only after being treated with a liquid latex sealant.

Subsequently, the fatigue limit of the bladders was investigated by cyclic squeezing of the SPSC using a pneumatic piston. In this case, the piston head functions as an infinitely rigid plate that exerts pressure on the specimen. During the cycle, the bladder transitions from the resting configuration $y_s = 0$ to the maximum squeezing configuration $y_s = y_{max}$.

Finally, a puncture test was performed using a conical probe made of Tough PLA, with tip diameter of 0.1 mm, half angle of 30 deg and a base diameter of 12 mm. This type of test is described in standards for evaluating the puncture resistance of protective clothing materials (e.g., plastics, coated fabrics, flexible materials) [2,19], and it is used in the literature to test the puncture resistance of rubber membranes [25]. In both fatigue and puncture tests, membrane damage was automatically detected by measuring the pressure inside the bladder, with a threshold value of $0.95\,p_i$.

These three tests were conducted on SPSCs made from four different materials, using Type B specimens of identical geometry for each material. Each test was repeated three times, and the mediated results are summarized in Table 2. In each test, the SPSCs were connected to the same rigid reservoir used for static characterization ($V_r = 40$ cm$^3$). The test bench used for this investigation is visible in Appendix E of supplementary material S1, together with microscopic details of damage incurred to SPSCs.

The silicone-molded bladder proved to be the most resistant in fatigue tests, reaching 5000 cycles without damage. However, it proved to be the most fragile to puncture, with a maximum force before failure of 27 N. If both fatigue tests and puncture tests are considered, the TPU 60A membrane fabricated via FDM proves to be the most reliable. SPSCs produced through compression molding exhibit high fatigue resistance but low puncture resistance, while SPSCs made from the same material using SLA demonstrate moderate fatigue resistance and high puncture resistance. Elastic 50A, on the other hand, proves to be particularly unreliable.

**Table 2**
Results of the destructive tests on the Type B SPSCs.

| Material | Fabrication process | Fatigue test[(1)] (cycles to failure) | Puncture test[(1)] (force to failure) |
|---|---|---|---|
| Easy Comp. AS40 | Compression molding | >5000[(2)] | 27 N |
| Recreus TPU 60A | FDM 3D print[(3)] | 4100 | 45 N |
| Formlabs Elastic 50A (cured) | SLA 3D print[(3)] | 1330 | 40 N |
| Formlabs Silicone 40A (cured) | SLA 3D print[(3)] | 2075 | >80 N[(2)] |

(1) The bladder supply pressure for this test is $p_i = 50$ kPa (gauge).
(2) The membrane has passed this test without rupture.
(3) The print plane is parallel to the plane $< \hat{i}, \hat{k} >$ reported in Fig. 2.

## 4. SPSC application in service robotics

The development of the sensing unit discussed above leads to a compliant unit that can be implemented in a robotic system to physically interact with the environment. The two primary applications that will be discussed are the usage of SPSCs in a compliant gripper with additional tactile sensing capabilities and a haptic device that interacts with the fingers of a human operator.

### 4.1. SPSC-based tactile sensing for robotic grasping

The interposition of a compliant element between the object to be grasped and the rigid gripper simplifies the grasping control, which shifts from a force to a position control [44]. Additional functionality relates to providing information on grasping operations, e.g., contact loss detection, stiffness identification, grasping force estimation, and object contouring [38]. While compliant solutions like Fin Ray and jamming-based grippers are common in the literature, they pose significant challenges for achieving such functionalities due to their inherent mechanical properties. Conversely, the variable stiffness SPSC-based system herein proposed is more easily suited to the integration of such advanced features, as it will be illustrated below.

Fig. 9 shows the architecture of PneuTact.Q, a system developed by the authors where SPSCs are used as soft fingertips for robotic grippers [6,7]. PneuTact.Q is designed as a plug-in system for the KG-2 two-finger gripper of the Kinova Gen2 7DoF manipulator.

In this application, grasping force is controlled via the coordinated action of the fingers and directional valves, and can be estimated by combining the pressure and contact area information. During the initial contact phase, the directional valve remains open until assessment of object properties, such as size and stiffness. Then, the valve is closed, and depending on the estimated object properties, the fingers are further closed (more in case of a rigid object) to increase the contact force and stabilize the grasp. It should be noted that this working logic, although using the sensing system in the low stiffness/low sensitivity condition to estimate object properties, is more robust. Indeed, reducing the SPSC

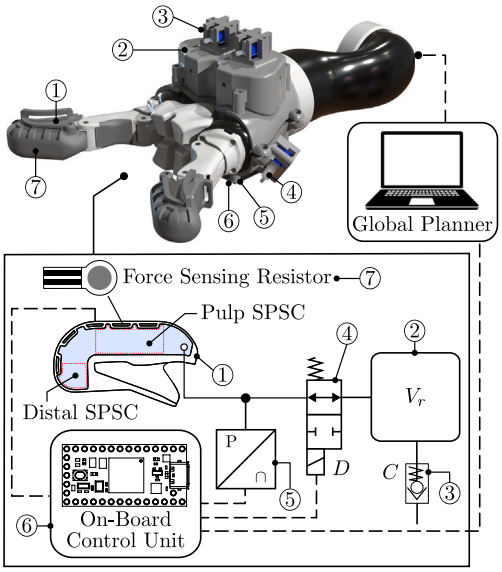


**Fig. 9.** PneuTact.Q: SPSC-based tactile sensing for advanced robotic manipulation capabilities. In this instance, two SPSCs (at the pulp and at the distal edge) are combined to create a single sensing chamber.

stiffness would result in a sudden pressure drop that would be indistinguishable from a contact loss. Thus, the system must be sensitive enough to infer object properties when in the low stiffness/low sensitivity mode.

The on-board control unit is responsible for collecting data from the SPSCs. The pressure inside the chambers is monitored through pressure sensors, one for each finger. To provide comprehensive contact information, five Force Sensing Resistors (FSRs) are also integrated on the surface of the sensing unit (three on the fingertip pulp, and two on the distal free edge). As a matter of fact, although pressure gives generalized information on contact, it lacks details on local contact, i.e., identical readings can be obtained from broad-shallow and small-deep contacts. Thus, FSRs are used to estimate the distribution of contact forces across the surface to provide data complementary to pressure.

The bladders have been manufactured in a monolithic design through SLA by using Formlabs Silicone 40A. The housings of FSRs are made through pockets, which protect the FSRs from potential damage caused by direct contact with the object [11]. A geometric coupling between the bladder and the finger was designed to rigidly fix the sensing unit to the gripper. Silicone 40A was chosen since it proved to be the most resistant to punctures, as shown in Section 3.2. This is generally useful because grasped objects can have sharp corners. Moreover, it is an SLA-printable material; thus the intricate monolithic design of the sensing unit can be realized effortlessly. The sensing unit is derived by combining two Type A SPSCs, located at the pulp and the distal edge of the fingertip, as shown in Fig. 9. These are connected via a lofted extrusion to form a single, unified chamber. While the high sensitivity requirements of the soft configuration might suggest Type D, Type A was selected for this application to provide a larger, flat upper surface to accommodate FSRs without excessive bending. Finally, the rear part of the tactile unit is made through a lofted extrusion to adapt to the surface of the gripper fingers.

The on-board control unit features a custom-made PCB integrated with a Teensy 3.2 microcontroller for signal I/O. A 2/2 NC solenoid valve (model 0520D, DC 24V, 80 mA, Foshan Weilizi Electronic Technology Co., Ltd.) is used as a check valve, and a modified 3/2 solenoid valve (model 0520F, DC 24V, 80 mA, Foshan Weilizi Electronic Technology Co., Ltd.), with an effective orifice area $\geq 0.3$ mm$^2$, serves as a 2/2 NO directional valve. Pressure measurements are acquired via Amphenol All Sensors ELVH-015G-HAND-C-NAA5 pressure sensors (F.S. 100 kPa gauge, $\pm 0.25\%$ accuracy). The FSRs (model FSR05BE, by Ohmite) have a circular active area with a diameter of 5.6 mm and a force range of up to 5 kg. Finally, the rigid reservoirs and the fixing masks are 3D-printed through FDM using Ultimaker Tough PLA. The complete sensing system has a total mass of approximately 230 g, which corresponds to 15% of the mid-range continuous payload of the manipulator, when equipped with the KG-2 two-finger gripper.

Fig. 10(a) shows experimental data acquired during the grasping of cylindrical objects of various sizes and stiffnesses. Here, the grasp detection is performed by setting threshold values on the pressure and its first derivative as a function of the finger closure angle $\alpha$. The value $\alpha_c$ represents, for all grasps, the angle at which contact with the object occurs. For these tests, directional valves on both fingers were open, i.e., both sensing units had low stiffness and low sensitivity. Once contact has been established, the compliance of the different objects becomes distinguishable after at least 10 deg of further finger closure. The dotted line was obtained by grasping the most rigid object, starting in a low stiffness configuration and then switching to high stiffness to stabilize the grasp.

Fig. 10(b) shows how slippage detection is performed by combining pressure and FSR data. Specifically, the slippage results in a pressure decrease and in a sliding of contact points towards the tip of the sensing unit. Then, when the object has slipped, there is a sudden increase in pressure produced by the fingers touching.

### 4.2. SPSC-based haptic interfaces

SPSC-based system can also be implemented as physical interface in haptic devices. Fig. 11 shows the architecture of an untethered haptic device, named PAL-HAND.Q by the authors. PAL-HAND.Q is a handheld joystick that consists of a rigid case, on which five variable stiffness SPSCs are positioned to serve as an interface between the device and the user fingers. In this application, a Type D SPSC made from TPU 60A is preferred for its higher pressure sensitivity and contact forces. The SPSC functionality is enhanced with an Eccentric Rotating Mass (ERM) mini vibration motor (model FIT0774, by DFRobot). To integrate the motor, the SPSC base is manually cut and re-joined, allowing the motor to be positioned against the inner top surface. Structural support for the

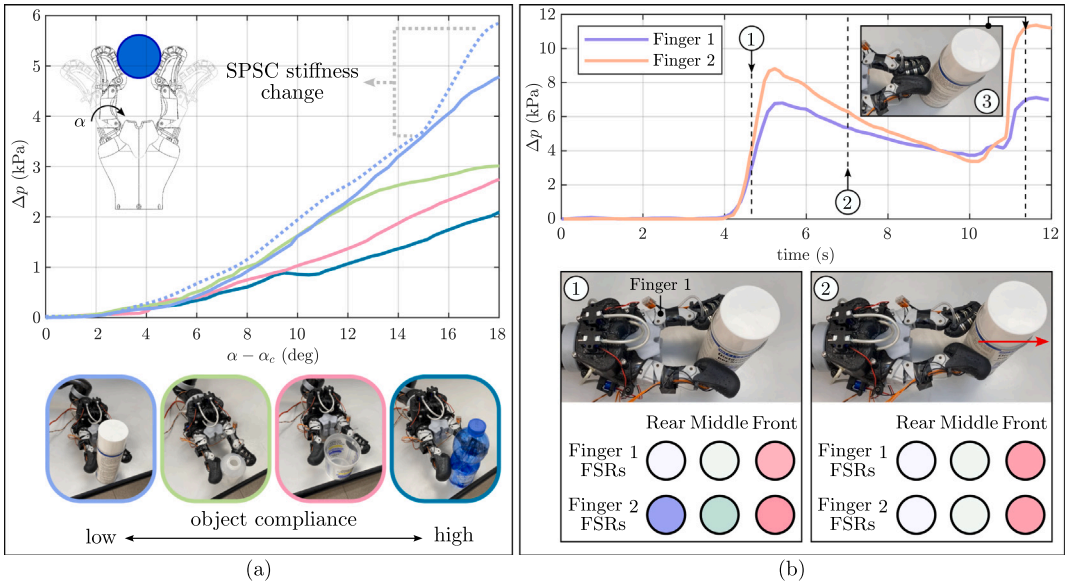


**Fig. 10.** (a) SPSCs pressure data are used to recognize the properties of different objects. Contact happens at finger angle $\alpha_c$, which depends on object size. The solid lines represent data obtained in the low stiffness/low sensitivity mode, while in the dotted line the SPSC stiffness change is used to stabilize the grasp of a rigid object. (b) Slippage detection is performed by combining pressure and FSR data. The slippage results in a pressure decrease and in a sliding of contact points towards the tip of the sensing unit. The brightness of FSRs colors is proportional to the intensity of contact, as measured by the FSR.

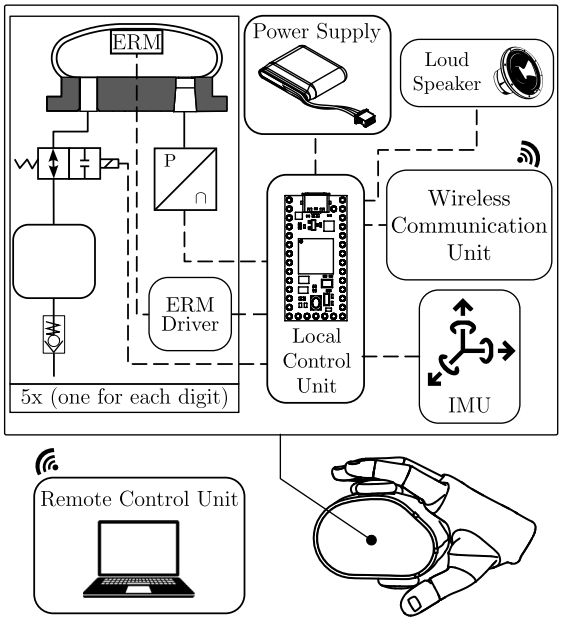


**Fig. 11.** PAL-HAND.Q: a handheld haptic device with kinesthetic and vibrotactile feedback enabled by SPSC-based interfaces.

ERM is provided by a thin TPU 60A film (0.8 mm thick), which is heat-bonded to the inner surface of the bladder to ensure secure placement. In this fashion, the SPSC can provide both force feedback, thanks to the auxiliary pneumatic system integrated into the device, and localized vibrotactile feedback, through the ERM. As shown in Fig. 11, the device also features a loudspeaker to provide acoustic feedback and an IMU (Inertial Measurement Unit) to track hand motion.

With a weight of approximately 500 g and dimensions of $160 \times 120 \times 100$ mm, PAL-HAND.Q leverages the proposed stiffness regulation system to balance functionality and lightness. This approach positions it uniquely among existing solutions. On one hand, it differs from complex wearable systems like the HaptX Glove G1 [15], which offer continuous stiffness regulation and comprehensive feedback but require bulky external components. On the other hand, it builds upon the capabilities of simpler handheld devices. While Squegg [36] and GripAble [14] provide data acquisition for the entire grasp, and Prohands Gripmaster [27] allows for individual finger exercise, PAL-HAND.Q offers a more advanced feature set. Specifically, it provides localized sensing, data acquisition, and a two-level stiffness regulation system for each individual finger.

The main intended field of application for PAL-HAND.Q is the active rehabilitation of people with upper limb impairments [5,8], as it is well established that the repetitive and voluntary execution of hand opening/closing actions significantly helps restore motor functionality of the limb [21] and also stimulates neuro-genesis [22]. To this end, input/output data collected by PAL-HAND.Q can be used to interact with desktop VR games to enhance user engagement during rehabilitation practices.

Fig. 12 demonstrates the use of the device to interact with a VR environment, developed through a custom graphics engine written in Python language using Pygame and ModernGL modules.

A preliminary calibration phase is conducted to set individual pressure thresholds: the user is instructed to compress each bladder with maximum effort while in the low-stiffness configuration; the activation threshold is defined as the sum of the pressure at rest and a fixed increment of 2% of the maximum pressure recorded during calibration. After calibration, the user interacts with the device to grasp and rotate a virtual object through the following sequence:

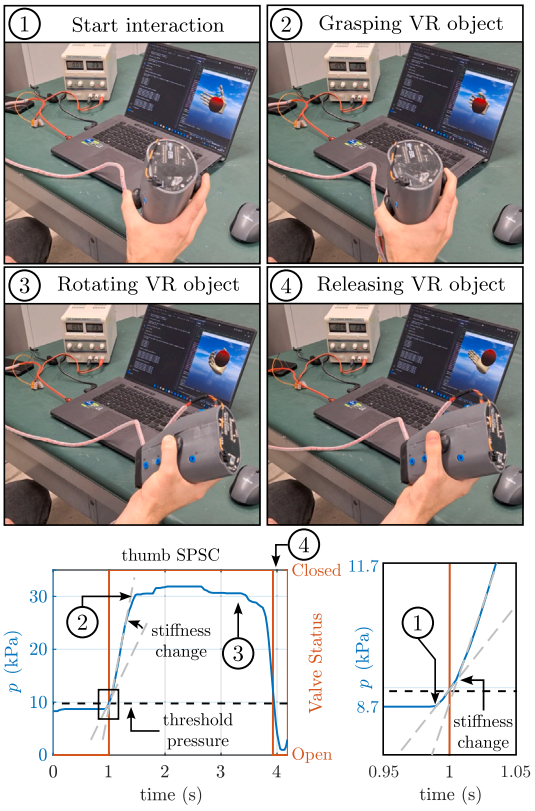


**Fig. 12.** Use of PAL-HAND.Q in a desktop VR environment. In this instance, the user performs a pick and place task. Contact with the object is simulated by switching the SPSC configuration from low to high stiffness.

1. initial engagement: the user begins pressing the bladders in a low-stiffness configuration (time instant ①). The pressure change is first calculated, then normalized against the maximum pressure change recorded during the calibration phase, and finally linearly mapped into rotation angles of the virtual fingers joints;
2. contact simulation: when the pressure within a specific SPSC exceeds the user-calibrated threshold, the corresponding digital valve is activated to increase the SPSC's stiffness, thereby simulating physical contact with the virtual object (time instant ②). This kinesthetic feedback is further reinforced by a vibration triggered on the corresponding phalanx;
3. manipulation: once all fingers establish contact, the user can manipulate the object's orientation by rotating the device (time instant ③). To maintain manipulation, the user must keep a pressure level above the threshold for each finger;
4. release and reset: finally, the user releases the virtual object in a new orientation, and the digital valves are switched back to the low-stiffness configuration (time instant ④).

As an example, Fig. 12 shows the pressure signal collected from the thumb bladder. As can be seen, there is a marked increase in the slope of the pressure signal following valve activation. Moreover, during interaction with the virtual object the pressure in the bladder remains above the calibrated threshold.

## 5. Conclusions

This paper presented the functional design, modeling, characterization, and application of variable stiffness Soft Pneumatic Sensing Chambers (SPSCs). The discrete regulation of the SPSC stiffness and sensitivity is achieved through a pneumatic auxiliary circuit connected to

the SPSC. The parameters affecting system stiffness and sensitivity have been identified, and four notable SPSC families (denoted as Types A-D) have been defined.

A numerical model has been applied to study the deformation of the SPSCs. It has been shown that both inflation and bulging of lateral walls significantly influence the SPSC performance, especially in the high stiffness configuration, and therefore cannot be disregarded in the modeling phase.

Static characterization of four SPSC samples revealed that Type D is optimal for applications requiring high sensitivity and contact forces. It has also been demonstrated that contact area and volume change data estimated from static tests can be used to predict the static performance across different setup pressures, thereby accelerating the characterization process.

The comparison between the numerical model and the experimental results showed a fairly good accordance for Types A and B, while further work is required to make the model more robust for Types C and D geometries.

Reliability testing showed that SPSCs fabricated from FDM 3D-printed TPU 60A offer a good trade-off between durability and resistance to sharp objects. In contrast, SLA 3D-printed Silicone 40A sacrifices some of this reliability, allowing the printing of more complex geometries.

Two applications of the proposed variable stiffness SPSCs have been discussed: tactile sensing for robotics and haptic devices for Human-Machine Interfaces. In these contexts, it has been demonstrated that the basic SPSC functionality can be enhanced by additional sensors and actuators directly integrated into the SPSC. These include Force Sensing Resistors (FSRs) for precise contact and slippage detection, and Eccentric Rotating Mass (ERM) motors for multi-modal haptic feedback.

Future research will focus on the shift from discretely-tunable to continuously-tunable stiffness. This problem should be solved by keeping the pneumatic auxiliary circuit compact and lightweight, which poses significant challenges in terms of system integration. Moreover, while this study mainly focused on the static performance of the SPSC system, future studies will focus on its dynamic performance. This will be critical for the development of proper control strategies in the case of continuous stiffness regulation.

## CRediT authorship contribution statement

**Simone Duretto:** Writing – original draft, Visualization, Software, Methodology, Investigation, Formal analysis, Data curation, Conceptualization. **Giovanni Colucci:** Writing – review & editing, Validation, Methodology, Investigation, Formal analysis, Conceptualization. **Luigi Tagliavini:** Writing – review & editing, Validation, Supervision, Formal analysis. **Andrea Botta:** Writing – review & editing, Validation, Supervision, Formal analysis. **Giuseppe Quaglia:** Writing – review & editing, Validation, Supervision, Project administration, Methodology, Conceptualization.

## Declaration of competing interest

The authors declare that they have no known competing financial interests or personal relationships that could have appeared to influence the work reported in this paper.

## Acknowledgment

This research is part of the project PNRR-NGEU which has received funding from the MUR – DM 117/2023.

## Appendix A. Supplementary data

Supplementary data to this article can be found online at doi:10.1016/j.sna.2026.117767.

## Data availability

Data will be made available on request.

## References

[1] P.N. Akella, M.R. Cutkosky, Contact transition control with semiactive soft fingertips, IEEE Trans. Robot. Autom. 11 (1995) 859–867, https://doi.org/10.1109/70.478432
[2] ASTM International, Standard test method for protective clothing material resistance to puncture, 2013. ASTM F1342-13.
[3] L. Biagiotti, P. Tiezzi, G. Vassura, C. Melchiorri, Modelling and Controlling the Compliance of a Robotic Hand with Soft Finger-Pads, vol. 4, Springer Berlin Heidelberg, Berlin, Heidelberg, 2005, pp. 55–73. https://doi.org/10.1007/11429555_4
[4] H. Choi, K. Kong, A soft Three-Axis force sensor based on radially symmetric pneumatic chambers, IEEE Sens. J. 19 (2019) 5229–5238, https://doi.org/10.1109/JSEN.2019.2904606
[5] G. Colucci, S. Duretto, G. Quaglia, A pneumatic HandHeld device for finger active Tele-Rehabilitation, in: New Trends in Medical and Service Robotics, Springer Nature Switzerland, Cham, 2025, pp. 378–387, https://doi.org/10.1007/978-3-031-96081-9_38
[6] G. Colucci, C. Visconte, G. Quaglia, Functional design and prototyping of a novel soft fingertip with variable stiffness, in: Proceedings of I4SDG Workshop 2023, Springer Nature Switzerland, Cham, 2023, pp. 278–289, https://doi.org/10.1007/978-3-031-32439-0_32
[7] S. Duretto, G. Colucci, A. Botta, L. Tagliavini, M. Jabari, L. Baglieri, L. Toccaceli, F. Amodio, G. Quaglia, Soft pneumatic sensing chambers for robotic grasping, in: Advances in Service and Industrial Robotics, Springer Nature Switzerland, Cham, 2025, pp. 164–173, https://doi.org/10.1007/978-3-032-02106-9_19
[8] S. Duretto, G. Colucci, M. Jabari, G. Quaglia, PAL-HAND.Q: a handheld device for bidirectional and multimodal haptic interaction, in: Advances in Italian Mechanism Science, Springer Nature Switzerland, Cham, 2024, pp. 483–491, https://doi.org/10.1007/978-3-031-64569-3_55
[9] O. Faris, C. Tawk, I. Hussain, SoPCAS finger: a Three-Dimensional printed soft finger with pneumatic chambers for simultaneous actuation, sensing, and controlled grasping, Robot. Rep. 2 (2024) 32–42, https://doi.org/10.1089/rorep.2023.0019
[10] W.W. Feng, W.-H. Yang, On the contact problem of an inflated spherical nonlinear membrane, J. Appl. Mech. 40 (1973) 209–214, https://doi.org/10.1115/1.3422928
[11] J.A. Fishel, V.J. Santos, G.E. Loeb, A robust micro-vibration sensor for biomimetic fingertips, in: 2008 2nd IEEE RAS & EMBS International Conference on Biomedical Robotics and Biomechatronics, 2008, pp. 659–663, https://doi.org/10.1109/BIOROB.2008.4762917
[12] A. Ghaffari, Y. Hojjat, A novel absolute rotary encoder based on soft pneumatic sensing chambers, IEEE Sens. J. 23 (2023) 1999–2007, https://doi.org/10.1109/JSEN.2022.3232540
[13] A. Ghaffari, Y. Hojjat, Simultaneous rotary and linear displacement sensor based on soft pneumatic sensing chambers, Sci. Rep. 14 (2024) 8317, https://doi.org/10.1038/s41598-024-59168-3
[14] GripAble Limited, GripAble device, 2025, https://gripable.co/ (accessed: 5 November 2025).
[15] HaptX Inc, HaptX gloves g1, 2025, https://haptx.com/gloves-g1/ (accessed: 5 November 2025).
[16] N. Hogan, Stable execution of contact tasks using impedance control, in: 1987 IEEE International Conference on Robotics and Automation Proceedings, 1987, pp. 1047–1054, https://doi.org/10.1109/ROBOT.1987.1087854
[17] J. Hughes, S. Li, D. Rus, Sensorization of a continuum body gripper for high force and delicate object grasping, in: 2020 IEEE International Conference on Robotics and Automation (ICRA), 2020, pp. 6913–6919, https://doi.org/10.1109/ICRA40945.2020.9196603
[18] J. Huo, H. Ru, B. Yang, X. Chen, X. Li, J. Huang, Air-Chamber-Based soft Six-Axis force/torque sensor for human–robot interaction, IEEE Trans. Instrum. Meas. 73 (2024) 1–12, https://doi.org/10.1109/TIM.2023.3338712
[19] International Organization for Standardization, Protective clothing – protection against cuts – test method using a moving blade, 1999. ISO 13997:1999.
[20] International Organization for Standardization, Ergonomics of human-system interaction, part 910: framework for tactile and haptic interaction, 2011. ISO 9241-910:2011.
[21] T.A. Jones, C.J. Chu, L.A. Grande, A.D. Gregory, Motor skills training enhances Lesion-Induced structural plasticity in the motor cortex of adult rats, J. Neurosci. 19 (1999) 10153–10163, https://doi.org/10.1523/JNEUROSCI.19-22-10153.1999
[22] G. Kempermann, H. van Praag, F.H. Gage, Chapter 3 activity-dependent regulation of neuronal plasticity and self repair, in: Functional Neural Transplantation II. Novel Cell Therapies for CNS Disorders, Elsevier. volume 127 of Progress in Brain Research, 2000, pp. 35–48, https://doi.org/10.1016/S0079-6123(00)27004-0
[23] N. Kuppuswamy, A. Alspach, A. Uttamchandani, S. Creasey, T. Ikeda, R. Tedrake, Soft-bubble grippers for robust and perceptive manipulation, in: 2020 IEEE/RSJ International Conference on Intelligent Robots and Systems (IROS), 2020, pp. 9917–9924, https://doi.org/10.1109/IROS45743.2020.9341534
[24] C. Lu, K. Tang, M. Yang, T. Yue, H. Li, N.F. Lepora, DexiTac: soft dexterous tactile gripping, IEEE/ASME Trans. Mechatron. 30 (2025) 333–344, https://doi.org/10.1109/TMECH.2024.3384432
[25] C.T. Nguyen, T. Vu-Khanh, J. Lara, Puncture characterization of rubber membranes, Theor. Appl. Fract. Mech. 42 (2004) 25–33, https://doi.org/10.1016/j.tafmec.2004.06.002
[26] B.Y. Ni, I. Elishakoff, C. Jiang, C.M. Fu, X. Han, Generalization of the Super ellipsoid concept and its application in mechanics, Appl. Math. Model. 40 (2016) 9427–9444, https://doi.org/10.1016/j.apm.2016.06.011

[27] Prohands Inc, Gripmaster Device, 2025, https://prohands.net/ (accessed: 5 November 2025).
[28] J. Qu, B. Mao, Z. Li, Y. Xu, K. Zhou, X. Cao, Q. Fan, M. Xu, B. Liang, H. Liu, X. Wang, X. Wang, Recent progress in advanced tactile sensing technologies for soft grippers, Adv. Funct. Mater. 33 (2023) 2306249, https://doi.org/10.1002/adfm.202306249
[29] E.R. Serina, E. Mockensturm, C.D. Mote, D. Rempel, A structural model of the forced compression of the fingertip pulp, J. Biomech. 31 (1998) 639–646, https://doi.org/10.1016/S0021-9290(98)00067-0
[30] G. Shi, A. Shariati, I. Eames, H. Wurdemann, Modelling the compression of a soft ellipsoid fingertip, Soft Matter 18 (2022) 9076–9085, https://doi.org/10.1039/D2SM00763K
[31] H.A. Sonar, J.-L. Huang, J. Paik, Soft touch using soft pneumatic actuator–skin as a wearable haptic feedback device, Adv. Intell. Syst. 3 (2021) 2000168, https://doi.org/10.1002/aisy.202000168
[32] M. Su, D. Huang, Y. Guan, C. Xiang, H. Zhu, Z. Liu, Soft tactile sensing for object classification and fine grasping adjustment using a pneumatic hand with an inflatable palm, IEEE Trans. Ind. Electron. 71 (2024) 3873–3883, https://doi.org/10.1109/TIE.2023.3279554
[33] C. Tawk, M. in het Panhuis, G.M. Spinks, G. Alici, Soft pneumatic sensing chambers for generic and interactive human–machine interfaces, Adv. Intell. Syst. 1 (2019) 1900002, https://doi.org/10.1002/aisy.201900002
[34] C. Tawk, M.I.H. Panhuis, G.M. Spinks, G. Alici, 3D printed soft pneumatic bending sensing chambers for bilateral and remote control of soft robotic systems, in: 2020 IEEE/ASME International Conference on Advanced Intelligent Mechatronics (AIM), 2020, pp. 922–927, https://doi.org/10.1109/AIM43001.2020.9158959
[35] C. Tawk, H. Zhou, E. Sariyildiz, M. in het Panhuis, G.M. Spinks, G. Alici, Design, modeling, and control of a 3D printed monolithic soft robotic finger with embedded pneumatic sensing chambers, IEEE/ASME Trans. Mechatron. 26 (2021) 876–887, https://doi.org/10.1109/TMECH.2020.3009365
[36] TheBioSparrow, Squegg device, 2025, https://www.mysquegg.com/ (accessed: 5 November 2025).
[37] H.X. Trinh, H.-H. Nguyen, T.-D. Pham, C.A. My, A novel rigid-soft gripper for safe and reliable object handling, J. Braz. Soc. Mech. Sci. Eng. 46 (2024) 176, https://doi.org/10.1007/s40430-024-04757-6
[38] L. Wang, Z. Wang, Mechanoreception for soft robots via intuitive body cues, Soft Robot. 7 (2020) 198–217, https://doi.org/10.1089/soro.2018.0135
[39] Z. Wang, R. Kanegae, S. Hirai, Circular shell gripper for handling food products, Soft Robot. 8 (2021) 542–554, https://doi.org/10.1089/soro.2019.0140
[40] M.S. Xavier, C.D. Tawk, Y.K. Yong, A.J. Fleming, 3D-printed omnidirectional soft pneumatic actuators: design, modeling and characterization, Sens. Actuators A: Phys. 332 (2021) 113199, https://doi.org/10.1016/j.sna.2021.113199
[41] H. Yang, Y. Chen, Y. Sun, L. Hao, A novel pneumatic soft sensor for measuring contact force and curvature of a soft gripper, Sens. Actuators A: Phys. 266 (2017) 318–327, https://doi.org/10.1016/j.sna.2017.09.040
[42] W.H. Yang, W.W. Feng, On axisymmetrical deformations of nonlinear membranes, J. Appl. Mech. 37 (1970) 1002–1011, https://doi.org/10.1115/1.3408651
[43] J. Yin, R. Hinchet, H. Shea, C. Majidi, Wearable soft technologies for haptic sensing and feedback, Adv. Funct. Mater. 31 (2021) 2007428, https://doi.org/10.1002/adfm.202007428
[44] T. Yoshikawa, Multifingered robot hands: control for grasping and manipulation, Annu. Rev. Control 34 (2010) 199–208, https://doi.org/10.1016/j.arcontrol.2010.09.001
[45] S. Zhao, C.C. Nguyen, T.T. Hoang, T.N. Do, H.-P. Phan, Transparent pneumatic tactile sensors for soft biomedical Robotics, Sensors 23 (2023), https://doi.org/10.3390/s23125671

## Author biography

**Simone Duretto** is a Ph.D. candidate at Politecnico di Torino, Italy, in the Department of Mechanical and Aerospace Engineering (DIMEAS). He received his Bachelor's and Master's degrees in Mechanical Engineering from Politecnico di Torino, in 2021 and 2023, respectively. His research interests include soft actuators, tactile sensors for robotic manipulation, and haptic technologies.

**Giovanni Colucci** is an Assistant Professor (RTDA) in the Department of Mechanical and Aerospace Engineering (DIMEAS) at Politecnico di Torino. He received his B.Sc. in Industrial Engineering in 2018 at Università del Salento in Lecce, his M.Sc. in Mechanical Engineering in 2021 and his Ph.D. in Mechanical Engineering in 2025 at Politecnico di Torino. His research activities regard Service Robotics and Soft Robotics.

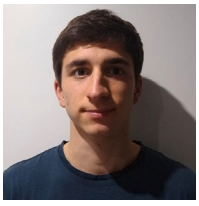

**Luigi Tagliavini** is an Assistant Professor (RTDA) in the Department of Mechanical and Aerospace Engineering (DIMEAS) at Politecnico di Torino, Italy. He received his B.Sc. in Mechanical Engineering in 2018 at Università degli Studi di Ferrara, his M.Sc. in Mechanical Engineering in 2020 at Politecnico di Torino, and his Ph.D. in Mechanical Engineering in 2024 at Politecnico di Torino. His research interest lies in the design and the development of innovative mobile service robots and assistive technologies.

**Andrea Botta** is assistant Professor (RTDA) at Politecnico di Torino, Italy. Enrolled as a student at Politecnico di Torino, he received his B.Sc. in Mechanical engineering in 2014, M.Sc. in Mechatronic Engineering in 2017, and Ph.D. in Mechanical Engineering in 2022 at Politecnico di Torino. In 2023, he held a postdoc position at Tokyo Institute of Technology funded by the Japanese Society for the Promotion of Science (JSPS) in 2023. His research activities are oriented towards sustainable development and the achievement of the Sustainable Development Goals. In particular, the research interest lies in the design and the development of innovative mobile service robots, with a focus on precision agriculture, and assistive and rehabilitative devices for the elderly, people with disabilities or people recovering from injuries.

**Giuseppe Quaglia** is a Full Professor of Applied Mechanics at Politecnico di Torino, Italy. His research activities focus on energy saving, renewable energy, sustainability, vehicle dynamics and systems, robotics and mechatronics, automation, actuators, and mechanisms. He is also actively involved in the development of devices for people with disabilities and biomedical applications, as well as technologies and systems that support sustainable human development. He serves as Chair of the Technical Committee for Sustainable Energy Systems of IFToMM, a member of the SIRI Council (Italian Association of Robotics and Automation), and a member of the Management Board of the PoliTO Interdepartmental Centre for Service Robotics (PIC4SeR). He also chairs IFToMM's Cross-Disciplinary Group 1: Securing Our Future Environment — Air, Water, Energy. In addition, he is the coordinator of the Inclusion and Equal Opportunities Green Team at Politecnico di Torino and the director of the Politecnico di Torino Japan Hub.